Mode-1 N_2 internal tides observed by satellite altimetry

Zhongxiang Zhao[1]

[1]Applied Physics Laboratory, University of Washington, Seattle, Washington, USA

Correspondence: Zhongxiang Zhao (zzhao@uw.edu)

Abstract. Satellite altimetry provides a unique technique for observing the sea surface height (SSH) signature of internal tides from space. Previous studies have constructed empirical internal tide models for major tidal constituents M_2, S_2, K_1, and O_1. Minor tidal constituents are difficult to observe, due to their weak SSH signals. The advances in mapping technique, combined with the accumulation of satellite altimetry data, make it possible to construct empirical models for minor internal tidal constituents. In this paper, the global mode-1 N_2 internal tides (the fifth largest oceanic tidal constituent) are observed using 100 satellite-years of SSH data from 1993 through 2019. This paper employs a newly-developed mapping procedure that includes two rounds of plane wave analysis and a two-dimensional bandpass filter in between. Thanks to the large SSH data set and the new mapping procedure, we can observe mode-1 N_2 internal tides with O (1 mm) SSH amplitudes. The results are confirmed using independent satellite altimetry data in 2020 and 2021. The satellite observations show that N_2 and M_2 internal tides have similar spatial patterns, and that the N_2 amplitudes are about 20% of the M_2 amplitudes. Both features mimic their barotropic counterparts. The satellite observations also show that N_2 and M_2 internal tides can propagate hundreds to thousands of kilometers in the open ocean, but at different phase speeds as predicted by theory.

1 Introduction

Internal tides are widespread in the ocean and affect numerous ocean processes (Wunsch, 1975; Whalen et al., 2020). Internal tides provide about half of the power for diapycnal mixing in the ocean interior (Munk and Wunsch, 1998; Egbert and Ray, 2000; MacKinnon et al., 2017; Kelly et al., 2021). It is important to study their generation, propagation, and dissipation, because the magnitude and geography of diapycnal mixing modulate the large-scale ocean circulation and global climate change (Jayne and St. Laurent, 2001; Melet et al., 2016; Pollmann et al., 2019; Vic et al., 2019; de Lavergne et al., 2020; Arbic, 2022). On the other hand, internal tides are annoying noise in the study of mesoscale and sub-mesoscale dynamics. In particular, the upcoming wide-swath SWOT (Surface Water and Ocean Topography) mission is designed to study the sub-mesoscale phenomena (Fu and Ubelmann, 2014; Morrow et al., 2019), one important task is to make internal tide correction to the SWOT data (Qiu et al., 2018; Wang et al., 2018). Empirical internal tide models can be constructed using past satellite altimetry sea surface height (SSH) measurements (Ray and Mitchum, 1996). However, previous satellite observations focus mainly on four major tidal constituents M_2, S_2, K_1, and O_1 (Dushaw, 2015; Ray and Zaron, 2016; Zhao et al., 2016; Zaron, 2019; Ubelmann et al., 2022). Dushaw (2015) attempts to map N_2 internal tides using the TOPEX/Poseidon data from 1992 to 2008, but the resulting N_2 internal tides are noisy (see his Figures 38 and 52), due to the short data set available then. In this paper, N_2 internal tides are

mapped using a large SSH data set by a new mapping procedure (Section 2). One main goal of this paper is to construct an N_2 internal tide model for SWOT.

The Moon's elliptical orbit around the Earth has an eccentricity of $\approx$0.055, with its perigean and apogean distances being about 3.63×10^5 and 4.06×10^5 km, respectively. The Moon completes one revolution every 27.5546 days (one anomalistic month). The tidal constituents L_2 and N_2 are reduced by the Moon's elliptical orbit (Doodson, 1921). They are named the smaller and larger lunar elliptical semidiurnal constituents. The L_2 and N_2 periods are 12.1916 and 12.6583 hours, respectively (Doodson, 1921; Pawlowicz et al., 2002). M_2 (12.4206 hours) is based on the mean distance between the Earth and the Moon (3.84×10^5 km). While the L_2 and N_2 superposition gives the 27.5546-day perturbation with the Moon-Earth distance changes along the elliptic orbit. On global average, the amplitudes of M_2, N_2, and L_2 have a respective ratio of 1 : 0.2 : 0.05. N_2 is the fifth largest tidal constituent (20% of M_2); therefore, its impact on the ocean environment is significant. For example, in waters around New Zealand, the N_2 barotropic tide has larger amplitudes than S_2 (Byun and Hart, 2020) (see their Figure 4). The superposition of N_2, M_2, L_2, and S_2 can cause perigean spring tides and apogean neap tides, which significantly affect harbors, coastal regions, and estuaries (Wood, 1978). Including N_2 internal tides can better parameterize the temporal variation of internal tide-driven ocean mixing with the Moon's elliptical motion.

The challenge of observing N_2 internal tides by satellite altimetry lies mainly in their weak SSH signals (Dushaw, 2015). Given that M_2 internal tides have SSH amplitudes of 1–2 cm, N_2 internal tides have only sub-centimeter-scale SSH amplitudes. In this paper, the observation of N_2 internal tides is made possible by two improvements. First, a large SSH data set becomes available, thanks to 27 years of accumulation from multiple satellite missions from 1993 through 2019 (Section 2.1). The merged SSH data set is about 100 satellite-years long; therefore, nontidal errors can be significantly suppressed. Second, a newly-developed mapping procedure is employed (Section 2.2). This new mapping technique extracts N_2 internal tides by taking advantage of their known theoretical wavelengths. Nontidal errors can be significantly suppressed by both temporal and spatial filtering. Although the resulting N_2 internal tides still have considerable errors, they can reveal the basic features of N_2 internal tides and work as a useful internal tide model. At present, it is extremely challenging to observe L_2 internal tides, which are estimated to have 1-mm SSH signals at most (5% of M_2).

The rest of this paper is arranged as follows. Section 2 describes the data and methods used in this paper. Section 3 presents and discusses the resulting N_2 internal tides, mainly by comparing with the well-studied M_2 internal tides. Section 4 is a summary.

2 Data and methods

2.1 Data

The satellite SSH data analyzed in this paper are measured by multiple satellite altimetry missions from 1993 through 2019. In the order of launch time, they are TOPEX/Poseidon, ERS-1, ERS-2, Geosat Follow-On, Jason-1, Envisat, Jason-2, CryoSat-2, SARAL/AltiKa, Haiyang-2A, Sentinel-3A, Sentinel-3B, and Haiyang-2B (Taburet et al., 2019; Abdalla et al., 2021). The new mapping technique can handle data from both exact-repeat and non-repeat missions (Zhao, 2022); thus, data from all previous

satellite altimetry missions are used in this paper. The combined data set is about 100 satellite-years long. The SSH measurements have been processed by standard corrections for atmospheric effects, surface wave bias, and geophysical effects (Pujol et al., 2016; Taburet et al., 2019). The ocean barotropic tide, polar tide, solid Earth tide and loading tide are corrected using theoretical or empirical models (Pujol et al., 2016). Furthermore, mesoscale correction is made using the AVISO (Archiving, Validation, and Interpretation of Satellite Oceanographic Data) gridded SSH fields (Ray and Byrne, 2010; Ray and Zaron, 2016; Zaron and Ray, 2018; Zhao, 2021). In this paper, the SSH data in 2020 and 2021 are used to evaluate the new N_2 internal tide model as independent data (Section 3.4).

2.2 Methods

The core technique of the new mapping procedure is plane wave analysis. By plane wave analysis, mode-1 N_2 internal tides are mapped using SSH data along discrete ground tracks onto a spatially regular grid (Zhao et al., 2016). In this paper, the fitting window is chosen to be 160 km by 160 km, consistent with wavelengths of mode-1 N_2 internal tides. The resulting N_2 internal tide field is at a $0.1°$ longitude by $0.1°$ latitude grid. Five mode-1 N_2 internal tidal waves are fitted at each grid point, and their sum gives the internal tide solution. One target internal tidal wave $\eta(A, \theta, \phi)$ has three parameters to be determined: amplitude A, phase ϕ, and propagation direction θ. They are fitted following

$$\eta = \Sigma_{m=1}^5 A_m \cos(k\, x \cos\theta_m + k\, y \sin\theta_m - \omega t - \phi_m), \tag{1}$$

where x and y are the east and north Cartesian coordinates, t is time, ω and k are the N_2 frequency and wavenumber, respectively (Zhao et al., 2016). Using all SSH measurements in one given fitting window, the amplitude A, phase ϕ, and propagation direction θ of one target internal tidal wave are determined by least-squares fit. After determining one wave, its signal is predicted and subtracted from the original data. This analysis can be repeated to determine another internal tidal wave. An iterative algorithm has been developed to extract five largest internal waves one by one. A detailed illustration of this method is given in Figure 2 of Zhao et al. (2016). The local wavenumber of mode-1 N_2 internal tides is obtained by solving the orthogonal equation using climatological hydrography in the World Ocean Atlas (WOA) 2018 (Boyer et al., 2018).

The N_2 internal tides are extracted following a three-step procedure, which includes two rounds of plane wave analysis and a spatial two-dimensional (2D) bandpass filter in between (Zhao, 2020, 2021, 2022). In the first step, the N_2 internal tides are mapped by plane wave analysis as described above. In the second step, the spatially regular N_2 internal tide field is cleaned by a 2D bandpass filter in overlapping 800 km windows. The internal tide field is first converted to the 2D wavenumber spectrum by Fourier transform. The spectrum is truncated to [0.85 1.20] times the local N_2 wavenumber. The truncated spectrum is converted back to the internal tide field by inverse Fourier transform (Zhao et al., 2019). In the third step, plane wave analysis is called again to decompose the filtered internal tide field into five internal waves of different propagation directions. The five waves are saved with their amplitudes, phases and propagation directions. They will be used to extract long-range internal tidal beams in the ocean (Section 3.2). An interested reader is referred to Zhao (2020, 2021, 2022) for a detailed description of the three-step procedure.

In this paper, mode-1 M_2 internal tides are constructed using the same data set and following the same procedure. The resulting M_2 internal tides are almost identical to those obtained in previous studies using slightly different SSH data sets (Zhao, 2021, 2022). A study of their small differences is not the focus of the present paper. In this paper, the new M_2 and N_2 internal tide models are compared for their similarities and differences.

3 Results

3.1 Global N_2 internal tides

Figure 1a shows the N_2 amplitudes in the logarithmic scale ranging from 0.4 mm to 6.4 mm. The satellite observations show that N_2 internal tides are widespread in the global ocean. In the Pacific Ocean, strong N_2 internal tides are observed in regions such as the Hawaiian Ridge, the French Polynesian Ridge, the western North Pacific, and the western South Pacific near Australia. In the Indian Ocean, N_2 internal tides are observed in the Madagascar-Mascarene region, the Bay of Bengal, the Arabian Sea, among others. In the Atlantic Ocean, N_2 internal tides are generated in regions including the Amazon River plume, the Azores Islands, and the Vitoria-Trindade Ridge. For comparison, Figure 1b shows the M_2 internal tides obtained from the same data set. Figures 1a and 1b show that the N_2 and M_2 internal tides have similar spatial patterns, and that the N_2 amplitudes are about 20% of the M_2 amplitudes. To stress the scale factor, their colormap maxima are different by a factor of five. The largest N_2 amplitudes are about 5 mm, compared to 20–30 mm for the M_2 internal tides. Figure 1 also shows that the N_2 internal tides are noisier than M_2, because their weak SSH signals are easily affected by model errors.

The spatial similarity and scale factor between N_2 and M_2 internal tides originate from their barotropic counterparts. To explain this point, the N_2 and M_2 barotropic tides are extracted from TPXO8 (Egbert and Erofeeva, 2002), and shown in Figures 1c and 1d, respectively. Their SSH amplitudes are shown by colors, and their co-phase contours (at an interval of 30°) are shown by black lines. One remarkable feature is that the N_2 and M_2 barotropic tides have similar spatial patterns, and that the N_2 amplitudes are about 20% of the M_2 amplitudes. Because N_2 and M_2 have close oscillation periods, they have same generations over rough topographic features. Indeed, Egbert and Ray (2003) show that the M_2 and N_2 barotropic-to-baroclinic conversion maps have similar spatial patterns, and that their amplitudes differ by a factor of about 25 (see their Figure 1). In the causative chain, N_2 and M_2 have similar spatial patterns and factor-of-five amplitudes for both barotropic and baroclinic tides.

3.2 N_2 internal tidal beams

To detect long-range N_2 internal tidal beams, the multi-wave interference field should be separately resolved into components of different propagation directions. As described in Section 2, five internal tidal waves have been determined at each grid point by plane wave analysis. Utilizing the five-wave fitted results, the N_2 internal tide field is divided into northward (0°–180°) and southward (180°–360°) components. Each component contains internal tidal waves with propagation direction falling in its given range. Figures 2a and 2b give the two decomposed internal tide components, showing well-defined N_2 internal tidal
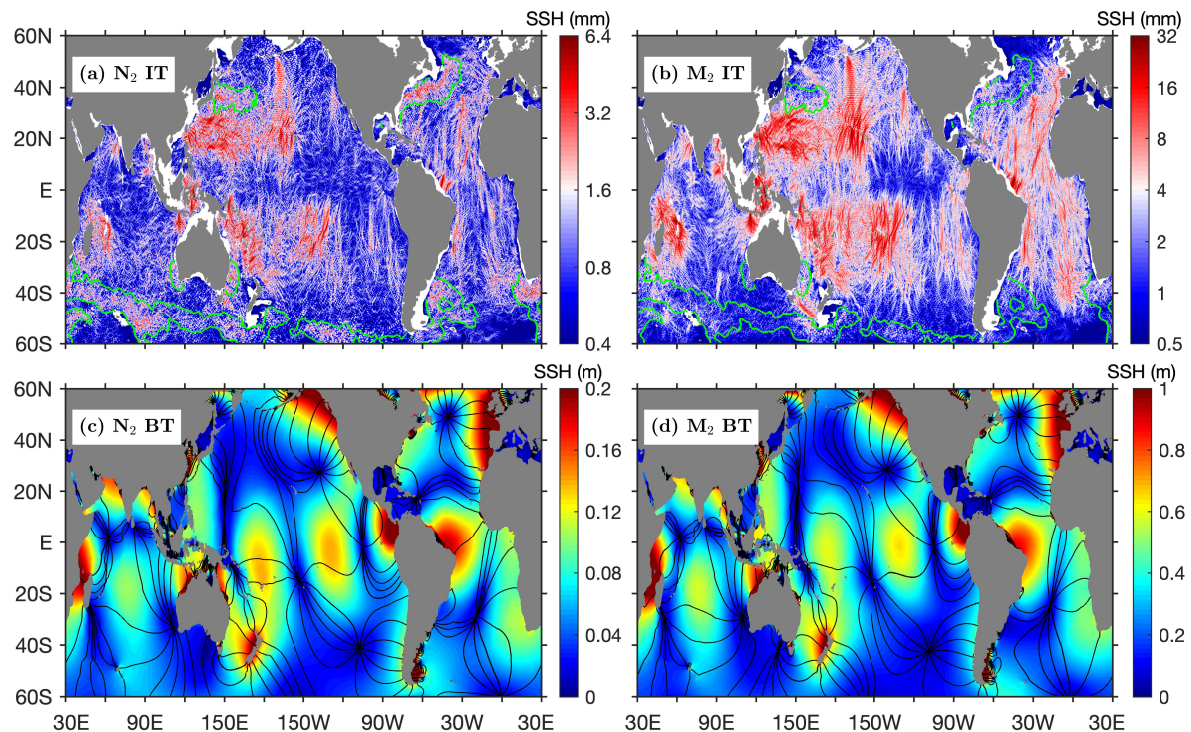
Figure 1. Global maps of (a) N_2 and (b) M_2 internal tides (IT) from satellite altimetry (this study) and (c) N_2 and (d) M_2 barotropic tides (BT) from TPXO8 (Egbert and Erofeeva, 2002). Green contours indicate regions of strong currents where both N_2 and M_2 have large errors. Black lines indicate co-phase contours at an interval of $30°$. For both barotropic and internal tides, N_2 and M_2 have similar spatial patterns and the N_2 amplitudes are about 20% of the M_2 amplitudes.

beams. Their $0°$ co-phase contours are shown in black line, with their neighboring intervals being one wavelength. One internal tidal beam has larger SSH amplitudes and parallel co-phase lines cross the beam. For example, one northward internal tidal

125 beam propagates from the Hawaiian Ridge to the Alaskan waters over 3,000 km (Figure 2a, bold black line). The southward beam from the Aleutian island chain can reach the Hawaiian Ridge about 3,000 km away (Figure 2b, bold black line). Figure 2 reveals a number of long-range N_2 internal tidal beams. Northward N_2 beams are observed to originate from the French Polynesian Ridge, the Macquarie Ridge, the Amazon River plume, and so on. Southward N_2 beams are observed to originate from the Andaman Islands, the Lombok Strait, the Hawaiian Ridge, the French Polynesian Ridge, the Mendocino Ridge, the

130 Azores Islands, among others.

Similarly, Figures 2c and 2d show the decomposed northward and southward M_2 internal tides. Long-range M_2 internal tidal beams are generated over the same sites as mentioned above. The M_2 beams have been discussed in previous studies (Zhao et al., 2016; Zhao, 2021, 2022). Further discussion is omitted here to avoid repetition. This paper stresses one remarkable feature: N_2 and M_2 have similar spatial distributions of long-range beams, as explained in Section 3.1. For the same reason,

135 their amplitudes are different by a factor of five. It is expected that both M_2 and N_2 internal tides can re-distribute the tidal

energy in the open ocean. Figure 2 also shows that the N_2 beams are generally shorter than the M_2 beams, because the weak

N_2 beams are prone to affected by background noise. The nontidal noise can be reduced in the future when more SSH data are

available (e.g., from SWOT).

3.3 Internal tide dispersion

140 The N_2 and M_2 internal tides disperse in long-range propagation, because of their different phase speeds. The propagation

speed, that is phase speed c_p, of internal tides follows (Gill, 1982)

$$c_p = \frac{\omega}{\sqrt{\omega^2 - f^2}} c, \qquad (2)$$

where ω and f are the tidal and inertial frequencies (due to the Earth rotation), respectively, and c is the eigenvalue speed

calculated from the WOA18 stratification profile. Equation (2) suggests that the phase speed is function of the tidal frequency

145 and latitude. At the equator (f=0), the N_2 and M_2 internal tides have the same phase speed. Off the equator, the N_2 internal

tides travel faster than M_2. Their percentage differences are 0.3%, 1.6% and 8.7% at 20°, 40°, and 60° latitude, respectively. It

also suggests that the N_2 and M_2 internal tides disperse with a higher degree at a higher latitude. For comparison, the dispersion

of M_2 and S_2 internal tides have been reported in previous studies (e.g., Zhao, 2017).

The N_2 and M_2 dispersion is demonstrated using their phase differences. For both the northward and southward components,

150 their point-wise phase differences are calculated. Figure 3 shows the resulting two global maps. The co-phase contours of the

N_2 internal tides are superimposed as black lines. Figure 3 shows that their phase differences are usually negative (blue) in

source regions, which are determined by relative phases of their barotropic counterparts. Leaving the source regions, their

phase differences increase with propagation, as evidenced by that blue becomes red. It is because N_2 internal tides travel faster

than M_2 internal tides. For the southward Aleutian beam, their phase difference increases from $-25°$ at 51°N to 210° at 28°N

155 (total change of 235°). For the northward Hawaiian beam, their phase difference increases from $-90°$ at 28°N to 110° at 52°N

(total change of 200°). From their co-phase contours, one can find that it takes about 18 tidal cycles for the N_2 and M_2 internal

tides to travel over the distance (about 3,000 km). Thus, their percentage differences are estimated to be 3.0–3.6%, within the

theoretical range of 0.5–4.0% in this latitudinal range.

3.4 Model evaluation

160 The N_2 internal tides can work as an empirical model to make internal tide correction for SWOT. Here this model is evaluated

using independent satellite altimetry data collected in 2020 and 2021. The evaluation method has been widely used in a

number of previous studies (Ray and Zaron, 2016; Zaron, 2019; Zhao, 2021; Carrere et al., 2021). For each SSH measurement

of known time and location, the N_2 internal tide signal is predicted using the model under evaluation, and subtracted from

the SSH measurement. Variance reduction is the variance difference before and after the internal tide correction. The variance

165 reductions for all SSH measurements are binned into 1° by 1° windows on a spatial grid of 1° longitude by 1° latitude. The

global map of variance reduction is shown in Figure 4a, and the variance of the N_2 internal tide model is shown in Figure 4b.
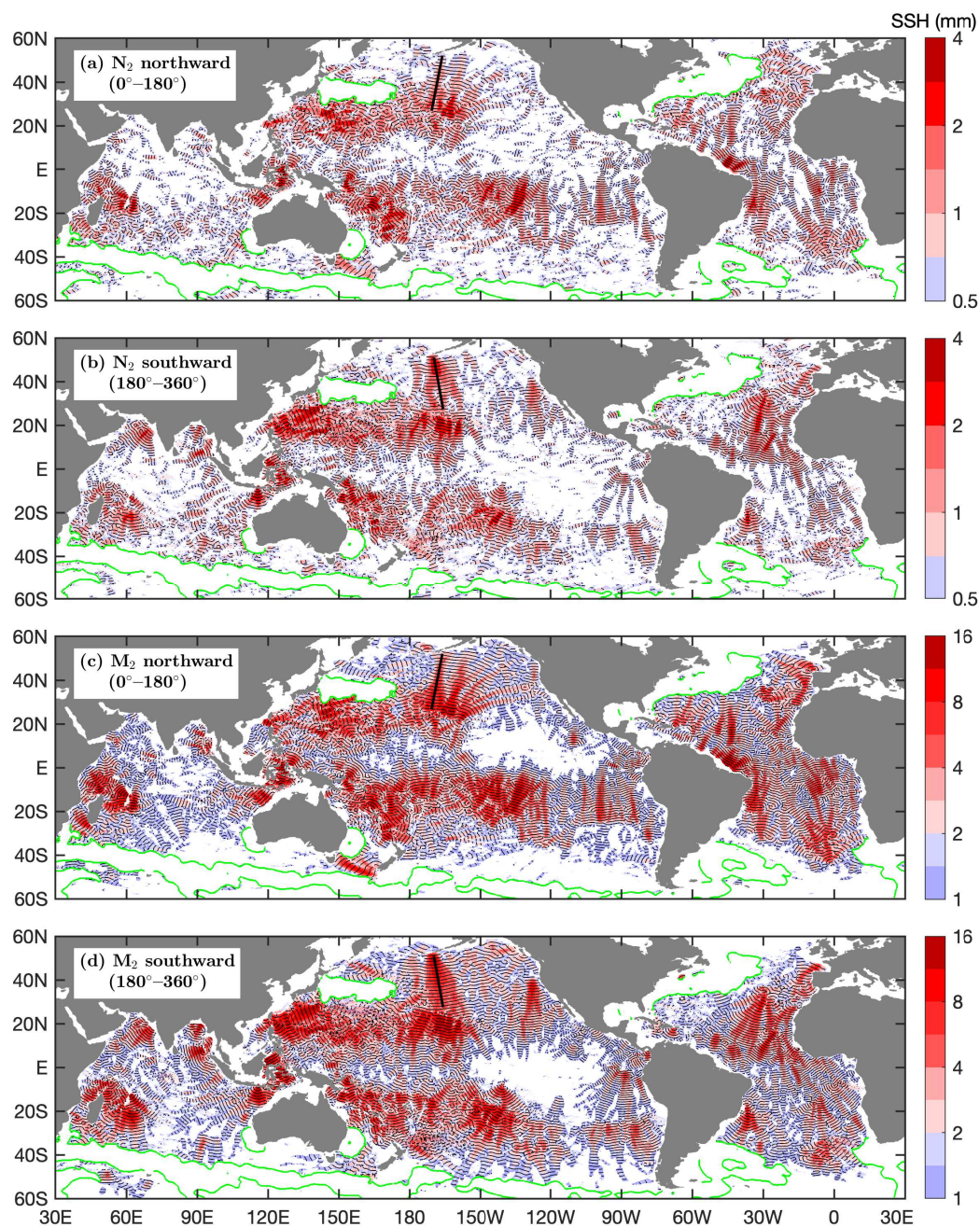
Figure 2. Long-range internal tidal beams. (a, b) N_2 internal tides. (c, d) M_2 internal tides. Both N_2 and M_2 constituents have been decomposed into northward ($0°-180°$) and southward ($180°-360°$) components. Colors show SSH amplitudes in the logarithmic scale. Black lines indicate $0°$ co-phase contours. Weak internal tides are discarded ($M_2 < 1$ mm; $N_2 < 0.5$ mm). Internal tides in shallow waters ($< 1,000$ m) or in regions of strong currents (green contours) are discarded. Bold black lines delineate two long-range internal tidal beams from the Hawaiian Ridge and the Aleutian island chain.
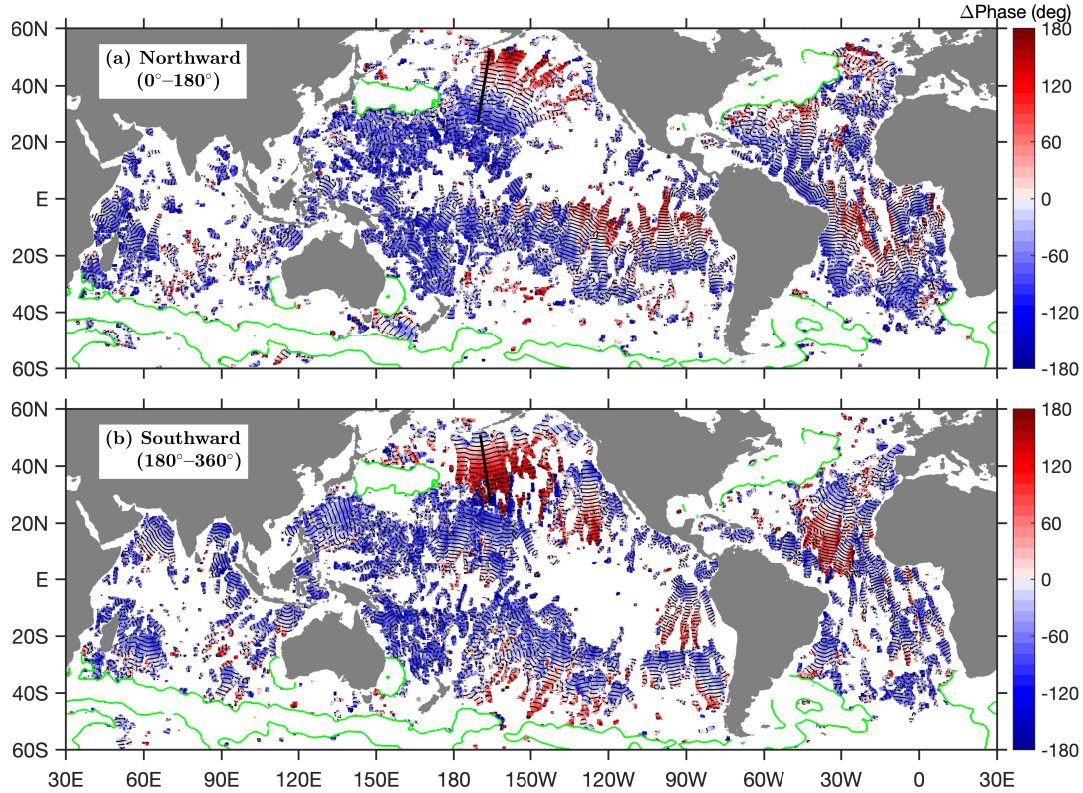
Figure 3. Phase differences between N_2 and M_2 internal tides. (a) Northward component. (b) Southward component. Colors show phase differences. Lines indicate the $0°$ co-phase contours of the N_2 internal tides. Phase differences of weak internal tides are discarded ($M_2 <1$ mm; $N_2 <0.5$ mm). Phase differences in shallow waters ($<1,000$ m) or in regions of strong currents (green contours) are discarded.

In regions of strong currents (green contours), the N_2 internal tides have large errors. The M_2 internal tide model is evaluated in the same way and shown in Figures 4c and 4d. In Figure 4, the colormap ranges of N_2 and M_2 are different by a factor of 25, that is, the square of the scale factor in amplitude.

170   In this evaluation method, the true N_2 internal tides in the model (variance σ_{N2}) will remove the N_2 internal tides in the independent data, leading to positive variance reduction. While the model errors (variance σ_ϵ) will increase the variance of the independent data, leading to negative variance reduction. Together, one obtains positive variance reduction where $\sigma_{N2} > \sigma_\epsilon$, and negative variance reduction where $\sigma_{N2} < \sigma_\epsilon$. Figure 4a shows that the global ocean is dominated by positive variance reduction, suggesting that the true N_2 internal tides are usually greater than model errors. In particular, in regions of strong N_2

175   internal tides such as the Hawaiian Ridge and the Amazon River plume, patches of positive variance reduction are observed, because the strong N_2 internal tides overcome model errors. For the same reason, negative variance reduction usually occurs in regions of weak N_2 internal tides such as the eastern equatorial Pacific and the Southern Ocean. The regions of strong currents (green contours) are dominated by negative variance reduction, where weak N_2 internal tides are overwhelmed by
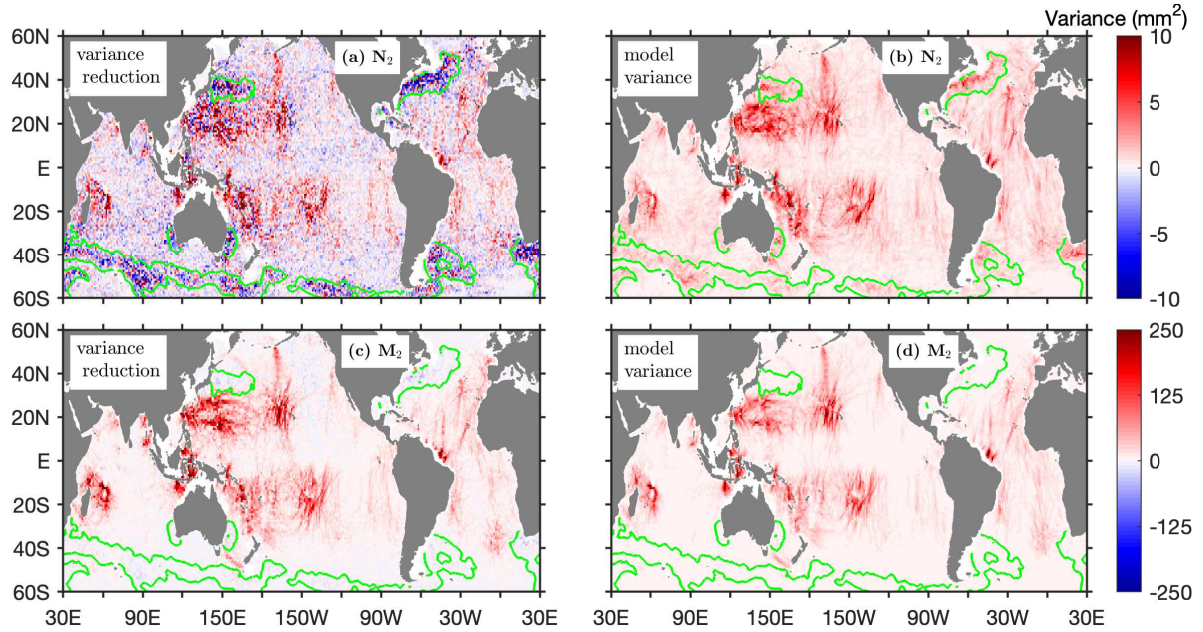
Figure 4. Model evaluation using independent satellite altimetry data in 2020 and 2021. (a, b) N_2 internal tides. (c, d) M_2 internal tides. Green contours indicate regions of strong currents where both N_2 and M_2 have large errors.

model errors. For comparison, Figure 4c shows that the M_2 internal tide model causes positive variance reduction throughout the global ocean, except for regions of strong currents (green contours). It is because the strong M_2 internal tides (five times of N_2) are usually greater than model errors $\sigma_{M2} > \sigma_\epsilon$. In summary, the empirical N_2 internal tide model can reduce variance in independent data, although the N_2 amplitudes are just a few mm. This evaluation confirms that the empirical N_2 internal tide model can make internal tide correction for SWOT, particularly in their source regions.

4 Summary

In the past, empirical internal tide models have been constructed using satellite altimetry data for major tidal constituents M_2, S_2, K_1, and O_1 (Carrere et al., 2021). In this paper, an empirical model is constructed for the fifth largest tidal constituent N_2. The larger lunar elliptical semidiurnal constituent N_2 is induced by the Moon's elliptical orbit. Its amplitudes are only about 20% of the M_2 amplitudes. The mode-1 N_2 internal tides have sub-centimeter-scale SSH amplitudes. We can observe the weak N_2 internal tides, thanks to (1) a large satellite altimetry data set and (2) a newly-developed mapping procedure. First, we use all satellite altimetry data from 1993 through 2019. The combined data set is about 100 satellite-years long, which can significantly suppress nontidal errors. Second, we extract N_2 internal tides by a newly-developed mapping procedure (Zhao, 2020, 2021, 2022). This new procedure cleans the internal tide field utilizing their known frequency and wavenumbers. As a result, satellite altimetry can observe N_2 internal tides with O (1 mm) SSH amplitudes. Note that the N_2 internal tides are

still noisy, due mainly to their weak signals. Future improvements can be made with more and more satellite altimetry data

195 becoming available. It is expected that other minor tidal constituents may be constructed by the same mapping procedure. In particular, the low-noise SWOT data along a 120-km swath will be very useful to observe the minor tidal constituents (Fu and Ubelmann, 2014; Morrow et al., 2019).

The satellite observations reveal some basic features of the global N_2 internal tides. We find that N_2 and M_2 internal tides have similar spatial patterns, and that the N_2 amplitudes are about 20% of the M_2 amplitudes. Both features mimic their

200 barotropic counterparts. In the causative chain, N_2 and M_2 internal tides have similar spatial patterns for the barotropic tide, the barotropic-to-baroclinic conversion, and internal tides. As such, this finding is useful for parameterizing the temporal variation of internal tide-driven ocean mixing with the lunar elliptical orbit cycle (27.5546 days). The satellite observations also show that N_2 and M_2 internal tides can propagate hundreds to thousands of kilometers in the open ocean, but they disperse in propagation due to their different phase speeds as expected by theory.

205 The newly-developed N_2 internal tide model is evaluated using independent satellite altimetry data in 2020 and 2021. The results show that the empirical model can significantly remove N_2 internal tides, and cause positive variance reduction, in particular, in regions of strong sources over topographic features. Therefore, the empirical N_2 internal tide model can make internal tide correction for SWOT, so that researchers can better study mesoscale and sum-mesoscale dynamics.

Data availability. The satellite altimetry along-track data were downloaded from the Copernicus Marine Service

210 (https://doi.org/10.48670/moi-00146). The satellite altimetry gridded data were also downloaded from the Copernicus Marine Service (https://doi.org/10.48670/moi-00148). The World Ocean Atlas 2018 is produced and made available by NOAA National Oceanographic Data Center (https://www.nodc.noaa.gov/OC5/woa18/). On acceptance of the manuscript, the M_2 and N_2 internal tide models developed in this study will be uploaded to one permanent website and made free available to the public.

Author contributions. This paper is completed by the sole author.

215 *Competing interests.* The author has declared there are no competing interests.

Acknowledgements. This study was funded by the National Aeronautics and Space Administration (NASA) via projects NNX17AH57G and 80NSSC18K0771.

References

Abdalla, S., Abdeh Kolahchi, A., Adusumilli, S., Aich Bhowmick, S., Alou-Font, E., Amarouche, L., Andersen, O. B., and co-authors: Altimetry for the future: Building on 25 years of progress, Advances in Space Research, 68, 319–363, https://doi.org/10.1016/j.asr.2021.01.022, 2021.

Arbic, B. K.: Incorporating tides and internal gravity waves within global ocean general circulation models: A review, Progress in Oceanography, 206, 102 824, https://doi.org/10.1016/j.pocean.2022.102824, 2022.

Boyer, T. P., García, H. E., Locarnini, R. A., Zweng, M. M., Mishonov, A. V., Reagan, J. R., Weathers, K. A., Baranova, O. K., Paver, C. R., Seidov, D., and Smolyar, I. V.: World Ocean Atlas 2018, Tech. rep., NOAA National Centers for Environmental Information, https://www.ncei.noaa.gov/archive/accession/NCEI-WOA18, 2018.

Byun, D.-S. and Hart, D. E.: A monthly tidal envelope classification for semidiurnal regimes in terms of the relative proportions of the S_2, N_2, and M_2 constituents, Ocean Science, 16, 965–977, https://doi.org/10.5194/os-16-965-2020, 2020.

Carrere, L., Arbic, B. K., Dushaw, B., Egbert, G. D., Erofeeva, S. Y., Lyard, F., Ray, R. D., Ubelmann, C., Zaron, E., Zhao, Z., Shriver, J. F., Buijsman, M. C., and Picot, N.: Accuracy assessment of global internal tide models using satellite altimetry, Ocean Science, 17, 147–180, https://doi.org/10.5194/os-17-147-2021, 2021.

de Lavergne, C., Vic, C., Madec, G., Roquet, F., Waterhouse, A. F., Whalen, C. B., Cuypers, Y., Bouruet-Aubertot, P., Ferron, B., and Hibiya, T.: A parameterization of local and remote tidal mixing, Journal of Advances in Modeling Earth Systems, 12, e2020MS002 065, https://doi.org/10.1029/2020MS002065, 2020.

Doodson, A. T.: The harmonic development of the tide-generating potential, Proceedings of the Royal Society A, 100, 305–329, https://doi.org/10.1098/rspa.1921.0088, 1921.

Dushaw, B. D.: An empirical model for mode-1 internal tides derived from satellite altimetry: Computing accurate tidal predictions at arbitrary points over the world oceans, Tech. rep., Applied Physics Laboratory, University of Washington, https://apl.uw.edu/project/projects/tm_1-15/pdfs/tm_1_15.pdf, 2015.

Egbert, G. D. and Erofeeva, S. Y.: Efficient inverse modeling of barotropic ocean tides, J. Atmos. Oceanic Technol., 19, 183–204, https://doi.org/10.1175/1520-0426(2002)019<0183:EIMOBO>2.0.CO;2, 2002.

Egbert, G. D. and Ray, R. D.: Significant dissipation of tidal energy in the deep ocean inferred from satellite altimeter data, Nature, 405, 775–778, https://doi.org/10.1038/35015531, 2000.

Egbert, G. D. and Ray, R. D.: Semi-diurnal and diurnal tidal dissipation from TOPEX/Poseidon altimetry, Geophysical Research Letters, 30, 1907, https://doi.org/10.1029/2003GL017676, 2003.

Fu, L.-L. and Ubelmann, C.: On the transition from profile altimeter to swath altimeter for observing global ocean surface topography, Journal of Atmospheric and Oceanic Technology, 31, 560–568, https://doi.org/10.1175/JTECH-D-13-00109.1, 2014.

Gill, A. E.: Atmosphere-Ocean Dynamics, Academic Press, 1982.

Jayne, S. R. and St. Laurent, L. C.: Parameterizing tidal dissipation over rough topography, Geophysical Research Letters, 28, 811–814, https://doi.org/10.1029/2000GL012044, 2001.

Kelly, S. M., Waterhouse, A. F., and Savage, A. C.: Global dynamics of the stationary M_2 mode-1 internal tide, Geophysical Research Letters, 48, e2020GL091 692, https://doi.org/10.1029/2020GL091692, 2021.

MacKinnon, J. A., Zhao, Z., Whalen, C. B., Waterhouse, A. F., Trossman, D. S., Sun, O. M., Laurent, L. C. S., Simmons, H. L., Polzin, K., Pinkel, R., Pickering, A., Norton, N. J., Nash, J. D., Musgrave, R., Merchant, L. M., Melet, A. V., Mater, B., Legg, S., Large, W. G., Kunze,

255   E., Klymak, J. M., Jochum, M., Jayne, S. R., Hallberg, R. W., Griffies, S. M., Diggs, S., Danabasoglu, G., Chassignet, E. P., Buijsman, M. C., Bryan, F. O., Briegleb, B. P., Barna, A., Arbic, B. K., Ansong, J. K., and Alford, M. H.: Climate process team on internal wave-driven ocean mixing, Bulletin of the American Meteorological Society, 98, 2429–2454, https://doi.org/10.1175/BAMS-D-16-0030.1, 2017.

Melet, A., Legg, S., and Hallberg, R.: Climatic impacts of parameterized local and remote tidal mixing, Journal of Climate, 29, 3473–3500, https://doi.org/10.1175/JCLI-D-15-0153.1, 2016.

260   Morrow, R., Fu, L.-L., Ardhuin, F., Benkiran, M., Chapron, B., Cosme, E., d'Ovidio, F., Farrar, J. T., Gille, S. T., Lapeyre, G., Le Traon, P.-Y., Pascual, A., Ponte, A., Qiu, B., Rascle, N., Ubelmann, C., Wang, J., and Zaron, E. D.: Global observations of fine-scale ocean surface topography with the Surface Water and Ocean Topography (SWOT) mission, Frontiers in Marine Science, 6, https://doi.org/10.3389/fmars.2019.00232, 2019.

Munk, W. H. and Wunsch, C.: Abyssal recipes II: Energetics of tidal and wind mixing, Deep-Sea Res. I, 45, 1977–2010,
265   https://doi.org/10.1016/S0967-0637(98)00070-3, 1998.

Pawlowicz, R., Beardsley, B., and Lentz, S.: Classical tidal harmonic analysis including error estimates in MATLAB using T_TIDE, Computers and Geosciences, 28, 929–937, 2002.

Pollmann, F., Nycander, J., Eden, C., and Olbers, D.: Resolving the horizontal direction of internal tide generation, Journal of Fluid Mechanics, 864, 381–407, https://doi.org/10.1017/jfm.2019.9, 2019.

270   Pujol, M.-I., Faugère, Y., Taburet, G., Dupuy, S., Pelloquin, C., Ablain, M., and Picot, N.: DUACS DT2014: the new multi-mission altimeter data set reprocessed over 20 years, Ocean Science, 12, 1067–1090, https://doi.org/10.5194/os-12-1067-2016, 2016.

Qiu, B., Chen, S., Klein, P., Wang, J., Torres, H., Fu, L.-L., and Menemenlis, D.: Seasonality in transition scale from balanced to unbalanced motions in the world ocean, Journal of Physical Oceanography, 48, 591–605, https://doi.org/10.1175/JPO-D-17-0169.1, 2018.

Ray, R. D. and Byrne, D. A.: Bottom pressure tides along a line in the southeast Atlantic Ocean and comparisons with satellite altimetry,
275   Ocean Dynamics, 60, 1167–1176, https://doi.org/10.1007/s10236-010-0316-0, 2010.

Ray, R. D. and Mitchum, G. T.: Surface manifestation of internal tides generated near Hawaii, Geophysical Research Letters, 23, 2101–2104, 1996.

Ray, R. D. and Zaron, E.: M_2 internal tides and their observed wavenumber spectra from satellite altimetry, Journal of Physical Oceanography, 46, 3–22, https://doi.org/10.1175/JPO-D-15-0065.1, 2016.

280   Taburet, G., Sanchez-Roman, A., Ballarotta, M., Pujol, M.-I., Legeais, J.-F., Fournier, F., Faugere, Y., and Dibarboure, G.: DUACS DT2018: 25 years of reprocessed sea level altimetry products, Ocean Science, 15, 1207–1224, https://doi.org/10.5194/os-15-1207-2019, 2019.

Ubelmann, C., Carrere, L., Durand, C., Dibarboure, G., Faugère, Y., Ballarotta, M., Briol, F., and Lyard, F.: Simultaneous estimation of ocean mesoscale and coherent internal tide sea surface height signatures from the global altimetry record, Ocean Science, 18, 469–481, https://doi.org/10.5194/os-18-469-2022, 2022.

285   Vic, C., Naveira Garabato, A. C., Green, J. A. M., Waterhouse, A. F., Zhao, Z., Melet, A., de Lavergne, C., Buijsman, M. C., and Stephenson, G. R.: Deep-ocean mixing driven by small-scale internal tides, Nature Communications, 10, 2099, https://doi.org/10.1038/s41467-019-10149-5, 2019.

Wang, J., Fu, L.-L., Qiu, B., Menemenlis, D., Farrar, J. T., Chao, Y., Thompson, A. F., and Flexas, M. M.: An observing system simulation experiment for the calibration and validation of the surface water ocean topography sea surface height measurement using in situ platforms,
290   Journal of Atmospheric and Oceanic Technology, 35, 281–297, https://doi.org/10.1175/JTECH-D-17-0076.1, 2018.

Whalen, C. B., de Lavergne, C., Naveira Garabato, A. C., Klymak, J. M., MacKinnon, J. A., and Sheen, K. L.: Internal wave-driven mixing: governing processes and consequences for climate, Nature Reviews Earth & Environment, https://doi.org/10.1038/s43017-020-0097-z, 2020.

Wood, F. J.: The strategic role of perigean spring tides: in nautical history and North American coastal flooding, 1635-1976, Department of Commerce, National Oceanic and Atmospheric Administration, National Ocean Survey, 1978.

Wunsch, C.: Internal tides in the ocean, Rev. Geophys. Space Phys., 13, 167–182, 1975.

Zaron, E. D.: Baroclinic tidal sea level from exact-repeating mission altimetry, Journal of Physical Oceanography, 49, 193–210, https://doi.org/10.1175/JPO-D-18-0127.1, 2019.

Zaron, E. D. and Ray, R. D.: Aliased tidal variability in mesoscale sea level anomaly maps, Journal of Atmospheric and Oceanic Technology, 35, 2421–2435, https://doi.org/10.1175/JTECH-D-18-0089.1, 2018.

Zhao, Z.: Propagation of the semidiurnal internal tide: Phase velocity versus group velocity, Geophysical Research Letters, 44, 11,942–11,950, https://doi.org/10.1002/2017GL076008, 2017.

Zhao, Z.: Southward internal tides in the northeastern South China Sea, Journal of Geophysical Research: Oceans, 125, e2020JC01 654, https://doi.org/10.1029/2020JC016554, 2020.

Zhao, Z.: Seasonal mode-1 M_2 internal tides from satellite altimetry, Journal of Physical Oceanography, 51, 3015–3035, https://doi.org/10.1175/JPO-D-21-0001.1, 2021.

Zhao, Z.: Development of the yearly mode-1 M_2 internal tide model in 2019, Journal of Atmospheric and Oceanic Technology, 39, 463–478, https://doi.org/10.1175/JTECH-D-21-0116.1, 2022.

Zhao, Z., Alford, M. H., Girton, J. B., Rainville, L., and Simmons, H. L.: Global observations of open-ocean mode-1 M_2 internal tides, Journal of Physical Oceanography, 46, 1657–1684, https://doi.org/10.1175/JPO-D-15-0105.1, 2016.

Zhao, Z., Wang, J., Menemenlis, D., Fu, L.-L., Chen, S., and Qiu, B.: Decomposition of the multimodal multidirectional M_2 internal tide field, Journal of Atmospheric and Oceanic Technology, 36, 1157–1173, https://doi.org/10.1175/JTECH-D-19-0022.1, 2019.